Electrochimica Acta 280 (2018) 41–54

Contents lists available at ScienceDirect

Electrochimica Acta

journal homepage: www.elsevier.com/locate/electacta

An integrated reduced order model considering degradation effects for $LiFePO_4$/graphite cells

Xinchen Zhao [a], Yalan Bi [a], Song-Yul Choe [a, *], Soo-Yeol Kim [b]

[a] Department of Mechanical Engineering, Auburn University, AL, 36849, USA
[b] KEPCO R&D Center, 105 Munji-ro, Yuseong-gu, Daejeon, 305-760, South Korea

ARTICLE INFO

Article history:
Received 22 January 2018
Received in revised form
17 April 2018
Accepted 13 May 2018
Available online 17 May 2018

Keywords:
Extended Kalman Filter
Lithium iron phosphate
Reduced order model
Side reaction

ABSTRACT

A reduced order model (ROM) considering degradation effects is proposed and validated against experiments for both fresh and cycled lithium iron phosphate (LFP)/graphite cells. The ion behaviors in the LFP particles such as two-phase transition and path dependence are modeled using a shrinking core with a moving interface between a lithium-rich and a lithium-deficient phase. The model errors are further minimized by employing the Extended Kalman Filter (EKF) to achieve a more accurate state-of-charge (SoC) estimation. The average error of SoC and voltage estimation is kept within 4% and 2%, respectively. Side reaction is regarded as the predominant cause of degradation, which can be accelerated by elevated temperatures, high SoC levels and large SoC cycling limits. The effects of operating conditions on degradation are described by a modified Butler-Volmer equation that is incorporated into the developed ROM. The integrated model facilitates to represent the degradation effects of side reaction, including loss of ions, loss of active material, growth of solid electrolyte interphase and deposit layer, and electrolyte decomposition. The model is capable of estimating capacity and power with an accuracy of 2% and 3% up to 1000 cycles, respectively.

1. Introduction

Lithium iron phosphate (LFP), firstly introduced by Padhi [1] et al., is a potential cathode material undergone remarkable developments in the commercial market of lithium ion batteries (LiBs), due to the characteristics of good electrochemical and thermal stability [2]. Compared with the electrodes embedded by Ni, Mn, Co, LFP based electrodes have the characteristics of two-phase transition and path dependence in both charge and discharge cycles. Srinivasan and Newman [3], Wang et al. [4] and Kavasajjula et al. [5] successively proposed a full order model (FOM) based on the concept of a shrinking core to simulate the discharge behaviors of both half and full cells with consideration of phase transformation rate, two-phase interface mobility and diffusion coefficients in both lithium-rich ($Li_{1-\beta}FePO_4$) and lithium-deficient phase ($Li_\alpha FePO_4$). The electrochemical behaviors of charge profiles were validated by incorporating Laudau transformation to generate a moving boundary [6]. In spite of high accuracy, complexity of the parameters and high computational efforts limit the real-time application of FOM. Plenty of reduction methods have been applied to reduce the execution time with accuracy maintained, such as single particle model (SPM) [7], enhanced SPM [8,9], state-variable model [10], reformulated model [11], proper orthogonal decomposition (POD) [12] model and volume averaging model [13]. However, the lack of predictive capability of end-of-life (EoL) performance impedes its use in the battery management system (BMS).

The degradation of LiBs corresponding to calendar life [14,15] and cycle life [16–19] is as the results of exposing to the ambient environment and cycling usage, respectively. The capacity and power fade are not caused by a single reason, but from large varieties. The inter-dependency of various degradation causes makes the comprehension of degradation mechanism more difficult. Schematic diagram of potential degradation mechanism taking place at composite electrodes, separator and current collectors is depicted in Fig. 1.

Degradation phenomena occurring at positive and negative electrode are significantly different. Researchers have identified the side reaction taking place at the interface between electrode and electrolyte at anode as the predominant cause of degradation for LiBs [20–30]. The main reaction is the intercalation/de-

* Corresponding author. 1418 Wiggins Hall, Auburn University, AL, 36849, USA.
E-mail address: choeson@auburn.edu (S.-Y. Choe).

https://doi.org/10.1016/j.electacta.2018.05.091
0013-4686/

Nomenclature

A	sandwich area of the cell (m^2)
a_s	specific surface area of electrode (m^{-1})
c	ion concentration (mol L^{-1})
D	diffusion coefficient(m^2 s^{-1})
F	Faraday constant (96,487 C mol^{-1})
I	current of the cell (A)
i_0	exchange current density of intercalation (Am^{-2})
j^{Li}	reaction rate of intercalation (Am^{-3})
k_s	isolation coefficient due to SEI
L	thickness of the micro cell (cm)
Q	capacity of the cell (Ah)
Q	amount of ion loss caused by side reaction (Ah)
R	resistance (Ω m^2) or universal gas constant (8.314 J mol^{-1} K^{-1})
R_s	radius of spherical electrode particle (m)
R	coordinate along the radius of electrode particle (m)
T	cell temperature (K)
t	time (s)
U	potential (V)
V	voltage (V) or volume of the composite electrode (m^3)
$\tilde{V}$	molar volume (m^3 mol^{-1})
x	stoichiometric number of the anode
y	stoichiometric number of the cathode

Greek symbols

α	transfer coefficient for an electrode reaction
δ	thickness (m)
ε	volume fraction of a porous medium
Φ	potential (V)
η	over-potential of electrode reaction (V)
κ	ionic conductivity (S m^{-1})
σ	conductivity (S m^{-1})

Subscripts and Superscripts

a	anodic
act	actual
aged	aged cell
ave	average value
c	cathodic
e	electrolyte phase
eff	effective
equ	equilibrium
error	error
exp	experiment
fresh	fresh cell
Li	lithium ion
main	main reaction
max	maximum
r	radial direction in electrode particle
s	solid phase
side	side reaction
sim	simulation
surf	electrode particle surface
0%	0% SoC
100%	100% SoC
+	positive electrode (cathode)
−	negative electrode (anode)
Θ	standard

intercalation of lithium ions to/from the electrode solid matrix during cycling. The side reaction takes place between the lithium ions and the electrolyte solvents, which leads to the formation of the unsolvable byproducts that are the main components of the solid electrolyte interphase (SEI) layer. The side reaction is described in Eqs. (1) and (2).

$$2Li^+ + 2e^- + EC \rightarrow CH_2{=}CH_2\uparrow + Li_2CO_3\downarrow \quad (1)$$

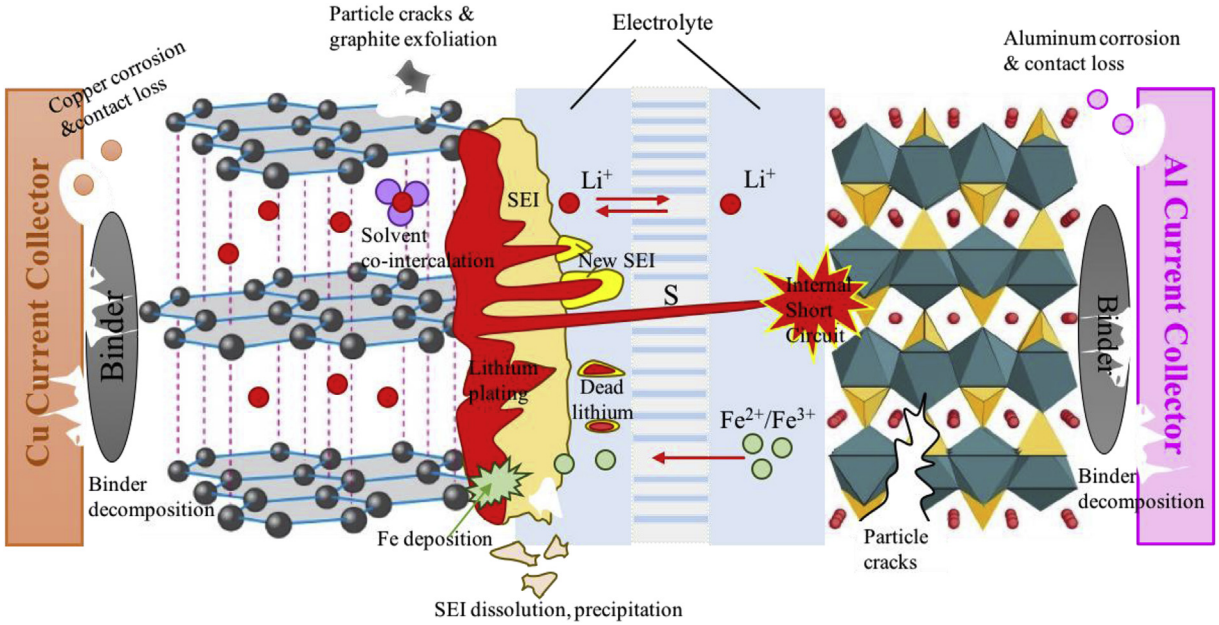

Fig. 1. Schematic diagram of degradation mechanism in LFP/graphite cells.

$$2Li^+ + 2e^- + 2EC \rightarrow CH_2 = CH_2\uparrow + (CH_2OCO_2Li)_2\downarrow \quad (2)$$

Other byproducts of the side reaction, such as LiOH, Li_2O, and ROLi etc., are neglected as minor components. The major compositions of the SEI after the reduction of ethylene carbonate (EC) based electrolyte are lithium carbonate (Li_2CO_3) and lithium ethylene dicarbonate ($(CH_2OCO_2Li)_2$). The SEI is prone to form at initial cycles, especially in charging protocol, which is used to protect the electrode from possible corrosion and prevent electrolyte from being decomposed. The SEI is permeable to lithium ions and electrolyte solvents, but impermeable to electrons, which can be treated as a natural barrier of the main reaction on the covered surface of anode. The schematic diagram of SEI formation at anode is shown in Fig. 2. The new SEI is formed at the interface between the pre-formed SEI and graphite particles. In addition, the SEI grows over time, clogs pores and isolates graphite particles that cause a decrease of the accessible area for lithium ions to participate in the reduction reactions, which provokes loss of active anode material. When the graphite particle is fully covered by the SEI, the isolation of electrons makes it impossible to participate in the chemical reaction anymore, which is treated as one source of the loss of recyclable lithium ions. The continuous consumption of lithium ions is the other source of loss of ions, which could result in capacity fade during prolonged cycles.

Previous study shows that the byproducts of side reaction are not only accumulated on the surface of graphite particles, but also on the interface between the composite anode and separator, which is defined as the deposit layer (DL) [31]. As the increasing thickness of the SEI and DL, the ionic conductivity decreases, which causes power fade. The continuous electrolyte decomposition and its attribute to side reaction leads to the impedance rise of electrolyte, which induces power fade as well. Thereby, loss of recyclable lithium ions and loss of active material (AM) of graphite electrode mainly result in capacity fade, while the impedance rise induced from the growth of SEI and DL and electrolyte decomposition are the main causes for power fade.

To degradation effects of LFP cathode, researchers [32–34] have identified iron deposition on the surface of graphite electrode by various characterization techniques, such as transmission electron microscopy (TEM) and Raman spectroscopy. It was also proposed that the iron dissolution from LFP electrode surface was caused by the chemical reaction between acidic species in the electrolyte and Fe^{3+} impurities [35]. In a failure case, the deposited irons on the surface of graphite electrode could grow as dendrites to cause internal short circuit. However, Liu et al. [36] revealed that the iron dissolution from LFP electrode was only a minor effect of degradation compared with those taking place on anode.

The various causes, impact factors and inter-dependencies of degradation mechanism make it extremely challenging to describe the degradation effects of LiBs mathematically. The models to predict the degradation phenomena can be divided into two groups, empirical/semi-empirical models [17,37–40] and physics-based electrochemical thermal models [41,42]. The models in the first group were developed by fitting the experimental data to obtain the empirical equations or extract degradation parameters to predict the capacity fade or impedance rise for both calendar life and cycle life. Even though it has the strengths of high accuracy, it is still limited by its high dependence on experimental data and empirical coefficients. In addition, the accuracy cannot be maintained if operating conditions are out of the experimental ranges. Conversely, the physics-based degradation models consider the side reaction whose rate was quantified by the reformulated Butler-Volmer (BV) equation based on the concept provided by Newman [43]. Considering the phase change phenomenon of LFP based cells, M. Safari and C. Delacourt [44,45] proposed a FOM incorporating side reaction based on the resistive-reactant perspective. The physical boundary between two phases was replaced by the concentration-dependent diffusion coefficients. P. Gambhire et al. [41] developed a ROM by volume averaging methods with concentration-dependent diffusivities and then incorporated SEI formation by side reaction. No capacity or power fade could be estimated in the abovementioned model.

In this paper, a physics-based ROM considering degradation effects were developed to estimate both beginning-of-life (BoL) and end-of-life (EoL) behaviors in real time. The integrated model was validated against experiments conducted by large-format pouch-type LFP/graphite cells. Due to the existence of the voltage plateau caused by two-phase transition on LFP electrode, the accuracy of SoC estimation was enhanced by incorporating a hybrid method combing both Extended Kalman Filter (EKF) and Coulomb counting. The degradation effects of side reaction, including ion loss, AM loss, SEI and DL growth, and electrolyte decomposition, were estimated. The capacity loss and power fade as a function of cycling time were also estimated by the model. The details of tests, including single cycles, multiple cycles for BoL and cycling tests for EoL are summarized in Section 2. The principles and equations of the electrochemical models are discussed in Section 3. Section 4 introduces the results of model validation against both fresh and cycled LFP/graphite cells. Section 5 is the conclusion.

2. Experiments

Cells used for experiments are the large-format pouch-type $LiFePO_4$/graphite cells provided by Top Battery, whose specifications are shown in Table 1. The LiBs are tested in a thermal chamber with three K-type thermocouples adhesive to the cell surface to measure temperatures. A programmable power supply and an

Table 1
Specifications of testing cells (provided by Top Battery).

Material	Cathode	LFP
	Anode	Graphite
	Electrolyte	Confidential
End-of-charge (EoC) voltage		3.6 V
End-of-discharge (EoD) voltage		2.0 V
Nominal capacity		20Ah

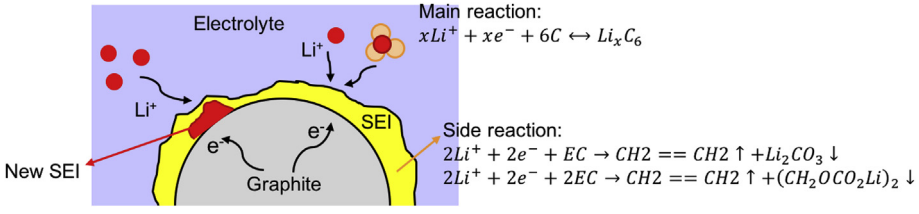

Fig. 2. Schematic diagram of SEI formation at anode.

electric-load are connected to supply the programmed charge/discharge current profiles. Impedance spectra are measured by electrochemical impedance spectroscopy (EIS) equipment, GAMRY, and the parameters are extracted by fitting the equivalent circuit model (ECM).

The experiments of fresh cells include measurement of the open-circuit voltage (OCV), application of the charge/discharge profiles in the single cycles and multiple cycles. The OCV is measured at the ambient temperature of 25 °C using a very small current of 0.05C-rate (1A) in order to allow the terminal voltage and OCV to be equal in the maximum likelihood. The charge/discharge protocols in the single and multiple cycles are as follows: 1) Pre-tests: 5 initial cycles at constant current (CC) of 1C-rate (20A) with 30 min' rest between each consecutive charge/discharge cycle; 2) Single-cycle tests: ① Charge the cell using CC until end-of-charge (EoC) voltage (3.6 V); ② Rest for 30 min; ③ Discharge the cell using CC until end-of-discharge (EoD) voltage (2 V). The CC applied at charging and discharging varies among 1C-rate, 2C-rate and 4C-rate at different ambient temperatures (25/40/55 °C, respectively). 3) Multiple-cycle tests: Discharge the cell to 2 V and then charge it to 3.6 V continuously without resting using CC at 1/2/4C-rate; 4) Post-tests: EIS and capacity measurements.

The test matrix of accelerated cycling tests is shown in Table 2. At every 30 or 60 cycles, the capacity and impedance are measured at 25 °C in the following steps. Capacity measurement: 1) Charge the cell using CC protocol (CC: 1C-rate) to 3.6 V; 2) Rest for 30 min; 3) Discharge the cell with 1C-rate CC to 2 V. EIS measurement: 1) Charge the cell to 50% SoC by 1C-rate CC; 2) Rest for 3 h; 3) Conduct EIS test at the frequency from 10 mHz to 1 kHz.

3. Model development

3.1. ROM

The single LFP/graphite cell is composed of multiple sandwich-structured microcells with three basic layers, composite anode, separator and composite cathode. The composite electrode is mainly fabricated by electrode particles, electrolyte and binder. When the cells are discharged, reduction and oxidation reactions take place at the anode and cathode, respectively. The lithium ions de-intercalated from the anode particles transport through the electrolyte to the cathode while the electrons transport through the external circuit. Likewise, the reverse reaction takes place at charging. The electrochemical behaviors, including intercalation/de-intercalation of lithium ions to/from the electrode, kinetics of chemical reaction taking place at the interface between electrode and electrolyte, ion transportation and diffusion through electrode particles and electrolyte, are described by the coupled partial differential equations (PDEs) which are solved by the finite difference method (FDM) in the FOM.

The mass transfer and charge conservation are governed by Fick's law and Ohm's law, respectively. The electrochemical kinetics are governed by the BV equation under consideration of both anodic and cathodic reactions. Due to the time-consuming demerits of the FOM, it is still necessary to simplify the governing equations in the FOM with decent accuracy maintained. The polynomial approach, state space approach and linearization are applied to reduce the order of the equations of ion concentration of electrode phase, ion concentration of electrolyte phase and current density, respectively. The ion behaviors of the two-phase transition and the existence of path dependence are considered by two set of parameters and number of layers coexisting in the LFP particles, respectively. The moving interfaces of the coexisting layers dependent upon the usage history has induced a moving boundary problem, or Stephen problem that describes the location of the boundary as a function of time and space, which can be solved by the variable space grid method. The governing equations and their corresponding boundary conditions of both FOM and ROM and the applied reduction methods are summarized in Table 3. The simplified governing equations of ion concentration in the solid particles are shown in Table 4.

Table 2
Test matrix.

T (°C)	Cha. Current	Dis. Current	⊿SoC		
			25–95%	5–75%	45–55%
25	4C-rate (80A)	4C-rate (80A)	1080 cycles 3000 cycles		3500 cycles
40			900 cycles		
55			870 cycles	540 cycles	
EIS test		Frequency range: 10 mHz to 1 kHz			

3.2. ROM with EKF

ROM can be used to estimate SoC calculated from the average ion concentration in the particles. However, the accuracy of SoC estimation is limited by the errors induced by the inaccuracy of the ROM, sensors and initial values of integration of the ion concentrations, which can be further minimized by using the EKF. The applied current and SoC are regarded as the input and output, respectively, where the average volume ion concentration of anode is regarded as a state and the terminal voltage is the measuring output. The principles of the EKF is summarized in Table 5.

When a current is applied to the battery, the difference between the measured and simulated terminal voltage is calculated at each time step and corrected by the optimized Kalman gain. Then the corrected error is feed-backed to update the state and the error covariance matrix (P). Finally, SoC is calculated using the average ion concentration of anode by Eq. (19). The process is carried out recursively and repetitively. The formulations of the EKF using ROM is shown in Table 6.

Since the SoC-OCV curve of LFP cells has a relatively flat region due to the characteristics of two-phase transition, the terminal voltage error is very small and might cause the EKF to stop updating and the Kalman gain to be zero, which is inevitable regardless of any controls. Therefore, a hybrid method of combining EKF and coulomb counting has been used. When the battery enters the stage of voltage plateau area, the SoC estimation algorithm switches from the EKF to coulomb counting. A tolerance is set to be the criteria of determining the SoC estimation mode. When the error of terminal voltage between the measured and estimated state is less than the tolerance, the algorithm used to do SoC estimation is coulomb counting and vice versa.

3.3. Physics-based degradation model

3.3.1. Model principles

In order to develop a physics-based degradation model, several assumptions have been made:

1. The byproducts of side reaction are only the mixture of Li_2CO_3 and $(CH_2OCO_2Li)_2$ based on Eq. (1) and Eq. (2).
2. The reduction reaction rate of side reaction is much higher than the oxidation reaction rate, which implies that the side reaction is an irreversible process.
3. Degradation effects on cathode, such as iron dissolution, are neglected.
4. No overcharge or undercharge process is considered.

Table 3
Governing equations of the FOM and ROM [46].

	FOM	Reduction method	ROM	
Ion concentration in electrode	$\frac{\partial c_s}{\partial t}=\frac{D_{s,\beta}}{r^2}\frac{\partial}{\partial r}\left(r^2\frac{\partial c_s}{\partial r}\right);\ D_{s,\beta}\frac{\partial c_s}{\partial r}\Big\vert_{r=r_1}=0$ $\frac{\partial c_s}{\partial t}=\frac{D_{s,\alpha}}{r^2}\frac{\partial}{\partial r}\left(r^2\frac{\partial c_s}{\partial r}\right);\ D_{s,\alpha}\frac{\partial c_s}{\partial r}\Big\vert_{r=R_s}=\frac{-j^{Li}}{a_sF}$ $(c_{s,\alpha\beta}-c_{s,\beta\alpha})\frac{dr_0}{dt}=D_{s,\beta}\frac{\partial c_{s,\beta}}{\partial r}\Big\vert_{r=r_0}-D_{s,\alpha}\frac{\partial c_{s,\alpha}}{\partial r}\Big\vert_{r=r_0}$	Polynomial approach	See Table 4	(3)
Ion concentration in electrolyte	$\frac{\partial(\varepsilon_e c_e)}{\partial t}=\frac{\partial}{\partial x}\left(D_e^{eff}\frac{\partial}{\partial x}c_e\right)+\frac{1-t_+^0}{F}j^{Li}$ $\frac{\partial c_e}{\partial t}\vert_{x=0}=\frac{\partial c_e}{\partial t}\vert_{x=L}=0$	State space approach	$\dot{\mathbf{c}}_\mathbf{e}=\mathbf{A}\cdot\mathbf{c}_\mathbf{e}+\mathbf{B}\cdot I$ $y=\mathbf{C}\cdot\mathbf{c}_\mathbf{e}+\mathbf{D}\cdot I$	(4)
Ohm's law in electrode	$\frac{\partial}{\partial x}\left(\sigma^{eff}\frac{\partial}{\partial x}\varphi_s\right)-j^{Li}=0$ $-\sigma^{eff}\frac{\partial}{\partial x}\varphi_s\Big\vert_{x=0}=-\sigma^{eff}\frac{\partial}{\partial x}\varphi_s\Big\vert_{x=L}=\frac{I}{A}$ $\frac{\partial}{\partial x}\varphi_s\Big\vert_{x=L_-}=\frac{\partial}{\partial x}\varphi_s\Big\vert_{x=L_-+L_{sep}}=0$	Finite difference method (FDM)	$\frac{\partial}{\partial x}\left(\sigma^{eff}\frac{\partial}{\partial x}\varphi_s\right)-j^{Li}=0$ $-\sigma^{eff}\frac{\partial}{\partial x}\varphi_s\Big\vert_{x=0}=-\sigma^{eff}\frac{\partial}{\partial x}\varphi_s\Big\vert_{x=L}=\frac{I}{A}$ $\frac{\partial}{\partial x}\varphi_s\Big\vert_{x=L_-}=\frac{\partial}{\partial x}\varphi_s\Big\vert_{x=L_-+L_{sep}}=0$	(5)
Ohm's law in electrolyte	$\frac{\partial}{\partial x}\left(\kappa^{eff}\frac{\partial}{\partial x}\varphi_e\right)+\frac{\partial}{\partial x}\left(\kappa_D^{eff}\frac{\partial}{\partial x}\ln c_e\right)+j^{Li}=0$ $\frac{\partial}{\partial x}\varphi_e\Big\vert_{x=0}=\frac{\partial}{\partial x}\varphi_e\Big\vert_{x=L}=0$	Ce has no influence on reaction current	$\frac{\partial}{\partial x}\left(\kappa^{eff}\frac{\partial}{\partial x}\varphi_e\right)+j^{Li}=0$	(6)
Electrochemical kinetics	$j^{Li}=a_s i_0\left\{\exp\left[\frac{\alpha_a F}{RT}\eta\right]-\exp\left[-\frac{\alpha_c F}{RT}\eta\right]\right\}$ $\eta=\varphi_s-\varphi_e-U_{equ}$	Linearization	$\frac{\partial}{\partial x}\left(\frac{\partial}{\partial x}\varphi_{se}\right)=j^{Li}\left(\frac{1}{\sigma^{eff}}+\frac{1}{k^{eff}}\right)$ $j^{Li}=\frac{a_s i_0 F}{RT}(\varphi_{se}-U)$	(7)

Table 4
Simplified governing equations of the ion concentration of solid phase.

	ROM equations	
$c_{s,surf}$	$\frac{\left(c_{s,surf}-c_{s,\beta\alpha}\right)(k_2-2k_1(r_s-r_0))-\left(c_{s,ave}-c_{s,\beta\alpha}\right)(2k_3(r_s-r_0)-k_4)}{k_2k_3-k_1k_4}=\frac{-j^{Li}}{a_sF}$	(8)
$c_{s,ave}$ of outer layer	$c_{s,ave0}^{k+1}\frac{4}{3}\pi\left(r_s^3-\left(r_0^{k+1}\right)^3\right)-c_{s,ave0}^{k}\frac{4}{3}\pi\left(r_s^3-\left(r_0^{k}\right)^3\right)$ $+c_{s,ave1}^{k+1}\frac{4}{3}\pi\left(r_0^{k+1}\right)^3-c_{s,ave1}^{k}\frac{4}{3}\pi\left(r_0^{k+1}\right)^3=\frac{-j^{Li}}{a_sF}4\pi r_s^2$	(9)
Interface	$\left(c_{s,\beta\alpha}-c_{s,\alpha\beta}\right)\frac{dr_0}{dt}=-D_{s,\beta}\frac{\left(c_{s,surf}-c_{s,\beta\alpha}\right)k_2-\left(c_{s,ave}-c_{s,\beta\alpha}\right)k_4}{k_2k_3-k_1k_4}$ $+\frac{D_s}{r_0}\left(35\left(c_{s,surf}-c_{s,ave}\right)-8q_{ave}r_0\right)$	(10)
$c_{s,ave}$ of inner layer	$\frac{d}{dt}c_{s,ave}-3\frac{D_s}{r_0^2}\left(35\left(c_{s,surf}-c_{s,ave}\right)-8q_{ave}r_0\right)=0$	(11)
q_{ave} of inner layer	$\frac{d}{dt}q_{ave}+\frac{1}{2}\frac{D_s}{r_0^2}(60q_{ave}r_0-45)\left(35\left(c_{s,surf}-c_{s,ave}\right)-8q_{ave}r_0\right)=0$	(12)
Notes	$k_1=\frac{3}{4}\left(\frac{r_s^4-r_0^4}{r_s^3-r_0^3}\right)-r_0,\ k_2=\frac{3}{5}\left(\frac{r_s^5-r_0^5}{r_s^3-r_0^3}\right)-\frac{3}{2}r_0\left(\frac{r_s^4-r_0^4}{r_s^3-r_0^3}\right),\ k_3=r_s-r_0,\ k_4=(r_s-r_0)^2$	

Table 5
Principles of EKF.

Prediction (Time update)	State prediction: $\hat{x}_k^-=f(\hat{x}_{k-1},u_{k-1})$ Error covariance prediction: $P_k^-=A_kP_{k-1}A_k^T+W_kQ_{k-1}W_k^T$	(13)
Correction (Measurement update)	Kalman gain: $K_k=P_k^-H_k^T(H_kP_k^-H_k^T+V_kP_{k-1}V_k^T)^{-1}$ State correction: $\hat{x}_k=\hat{x}_k^-+K_k(z_k-h(\hat{x}_k^-))$ Error covariance correction: $P_k=(1-K_kH_k)P_k^-$	(14)
Note	$A=\left.\frac{\partial f}{\partial x}\right\|_{x_{k-1}},W=\left.\frac{\partial f}{\partial w}\right\|_{w_{k-1}}$ $H=\left.\frac{\partial h}{\partial x}\right\|_{x_k},V=\left.\frac{\partial h}{\partial w}\right\|_{w_k}$	(15)

Table 6
Formulations of EKF using ROM.

State and measurement	$x=\left[\overline{c_{s,ave}^-}\right]$ $y=[V_t]$	(16)
System	$\overline{c_{s,ave}^-}^k=\overline{c_{s,ave}^-}^{k-1}-\frac{3j^{L1}I}{R_sa_sFAL^-}$ $V_t=U^+(\overline{y})-U^-(\overline{x})-\eta$	(17)
Jacobians	$A=I$ $H=\frac{\partial V_t}{\partial\overline{c_{s,ave}^-}}=\frac{\partial U_{OCV}^+}{\partial\overline{y}}\frac{\partial\overline{y}}{\partial\overline{c_{s,ave}^+}}\frac{\partial\overline{c_{s,ave}^+}}{\partial\overline{c_{s,ave}^-}}-\frac{\partial U_{OCV}^-}{\partial\overline{x}}\frac{\partial x}{\partial\overline{c_{s,ave}^-}}$	(18)
SoC estimation	$SoC=\left[\frac{1}{L^-}\int_0^{L^-}\frac{\left(c_{s,ave^-}-c_{s,max}\cdot x_0\right)}{c_{s,max}\cdot(x_{100}-x_0)}\cdot dx\right]\cdot 100\%$	(19)

5. No mechanical failure, such as graphite exfoliation, electrode volume change and particle cracks, is considered.

In the former developed ROM with EKF, the BV equation of Eq. (7) only describes the kinetics of main reaction. Considering side reaction, the BV equation is reformulated to describe the total reaction rate which is the sum of the reaction rate of the main and side reaction. Based on the assumptions above, the side reaction rate only considers the reduction reaction. The corresponding equations about degradation are summarized in Table 7. Compared to the over-potential of Eq. (7), the potential drop caused by SEI formation has been added in the model.

The equilibrium potential of main reaction,U_{equ}, is a function of the stoichiometric number and ion concentration in electrolyte according to the Nernst equation where U_{equ-}^{Θ} and U_{equ+}^{Θ} are the standard equilibrium potential of anode and cathode when $c_e=c_{e0}$, respectively. The equilibrium potential of cathode, U_{equ+}, is estimated by an empirical equation derived from Ref. [2]. Then the equilibrium potential of anode, U_{equ-}, can be calculated by the difference between measured OCV and U_{equ+}. However, the standard equilibrium potential of the side reaction, $U_{equ,side}^{\Theta}$, is no longer

Table 7
Equations for physics-based degradation model.

	Main reaction	Side reaction
Reaction rate	$j^{Li} = a_s i_0 \frac{(\alpha_a + \alpha_c)\cdot F}{RT}\eta$	$j^{Li}_{side} = -i_{0,side} a_s \exp\left(-\frac{\alpha_{c,side} n_{side} F}{RT}\eta_{side}\right)$
Over-potential	$\eta = \phi_s - \phi_e - U_{equ} - \frac{R_{SEI}}{a_s} j^{Li}_{total}$	$\eta_{side} = \varphi_s - \varphi_e - U_{equ,side} - \frac{R_{SEI}}{a_S} j^{Li}_{total}$
Equilibrium potential	$U_{equ-} = U^{\Theta}_{equ-}(x) + \frac{RT}{nF}\ln\left(\frac{c_{e-}}{c_{e0}}\right) U_{equ+} = U^{\Theta}_{equ+}(y) + \frac{RT}{nF}\ln\left(\frac{c_{e+}}{c_{e0}}\right)$	$U_{equ,side} = U^{\Theta}_{equ,side} + \frac{RT}{n_{side}F}\ln\left(\frac{c_e}{c_{e0}}\right)$
Total reaction rate	$j^{Li}_{total} = j^{Li} + j^{Li}_{side}$	
Notes [2]	$U_{equ+}(y) = 3.4323 + 0.8428\exp(-80.2493y^{1.3198}) + 3.2474\times10^{-6}\exp(20.2645y^{3.8003}) - 3.2482\times10^{-6}\exp(20.2646y^{3.7995})$	

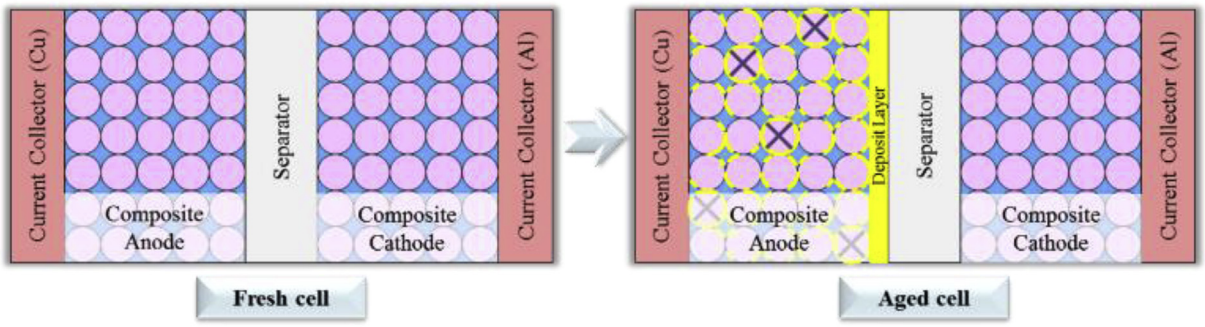

Fig. 3. Schematic diagram of degradation mechanism at anode of a microcell.

a function of the stoichiometric number, but depends on the material composition of the electrolyte. Various recommendation values of $U^{\Theta}_{equ,side}$ are provided by Ref. [24], such as 2 V, 1.7 V, 0.8 V and 0.4 V. The specific value of $U^{\Theta}_{equ,side}$ in this model is obtained by fitting experimental data of terminal voltage at various operating conditions.

3.3.2. Analysis of the effects of side reaction

The degradation effects of LiBs are inextricably linked to the side reaction. The schematic diagram of degradation mechanism is depicted in Fig. 3. Loss of recyclable lithium ions, loss of AM, growth of SEI and DL and electrolyte decomposition pertaining to main degradation effects are considered in the physics-based degradation model. The yellow shade in Fig. 3 denotes the byproducts of the side reaction, which are the major components of SEI and DL. The byproducts located at the interface between graphite particles and electrolyte are SEI, which partially or fully covers the particle surface. The DL is defined as a layer composed of the byproducts that are prone to accumulate at the interface between the composite anode and the separator. The particles with marker "X" represent the totally isolated electrode particles which cannot be involved in any further chemical reaction.

The degradation effects resulting from the side reaction can be discussed from two aspects, the consumption of the reactants and the aggregation of the products. With regard to the analysis of the reactants, the amount of consumed lithium ions in the side reaction can be calculated by integrating the side reaction rate over time and volume of the composite anode.

$$q^{Li}_{side}(t) = \int_{x=0}^{\delta_-}\left(\int_{\tau=0}^{t} j^{Li}_{side}(x,\tau)d\tau\right)Adx \tag{20}$$

where q^{Li}_{side} is the amount of consumed lithium ions with a unit of Ah. δ_- is the thickness of the composite anode. A denotes the cross section area of the LiB.

The consumption of the electrolyte solvent is analyzed by the change of the volume fraction of electrolyte, given by Eq. (21).

$$\frac{\partial\varepsilon_e}{\partial t} = -\frac{\alpha\tilde{V}_e}{\delta_- F}\int_{x=0}^{\delta_-} j^{Li}_{side}dx \tag{21}$$

where ε_e is the volume fraction of electrolyte solvent. $\tilde{V}_e$ is the molar volume of the electrolyte. α is a dimensionless coefficient indicating how many moles of the electrolyte solvents are involved in the side reaction when one mole of the lithium ions is consumed.

Provided that the byproducts of the side reaction are only Li_2CO_3 and $(CH_2OCO_2Li)_2$, the consumed molars of the electrolyte solvent are 0.5 and 1, respectively. Under the assumption of the same reaction rate for Eq. (1) and Eq. (2), α equals to 0.75. Correspondingly, the decrease of the volume fraction of the electrolyte solvents leads to a decrease of the effective diffusion coefficient in the electrolyte.

$$D^{eff}_e = D_e\cdot\varepsilon_e \tag{22}$$

The increasing rate of the SEI thickness is proportional to the reaction rate of the side reaction, given in Eq. (23).

$$\frac{\partial\delta_{SEI}}{\partial t} = -\frac{\tilde{V}_{SEI}}{2a_s F} j^{Li}_{side} \tag{23}$$

where δ_{SEI} and $\tilde{V}_{SEI}$ are the thickness and molar volume of the SEI layer, respectively.

The resistance increase of the SEI layer is given in Eq. (24).

$$\Delta R_{SEI} = \delta_{SEI}/\kappa_{SEI} \tag{24}$$

where κ_{SEI} is the ion conductivity of the SEI.

The growth of the SEI layer limits the accessible area of composite electrode, which causes the loss of AM, described in Eq. (25).

Table 8
Model parameters for BoL.

Category	Parameter	Negative electrode	Separator	Positive electrode	unit
Geometry and volume fractions	Thickness, δ	72×10^{-6}	20×10^{-6}	108×10^{-6}	m
	Particle radius, R_s	3.72×10^{-6}		0.475×10^{-6}	m
	Active material volume fraction, ε_s	0.5814		0.5589	
	Polymer phase volume fraction, ε_p	0.0369	0.5464	0.0243	
	Conductive filler volume fraction, ε_f	0.0069		0.0243	
	Porosity, ε_e	0.3749	0.4536	0.3925	
Li^+ concentrations	Stoichiometry at 0% *SOC*: $x_{0\%}$, $y_{0\%}$	0.02		0.84	
	Stoichiometry at 100% *SOC*: $x_{100\%}$, $y_{100\%}$	0.94		0.16	
	Average electrolyte concentration, c_e	1.2×10^3	1.2×10^3	1.2×10^3	mol m^{-3}
	Exchange current density coefficient, i_0	13.2×10^4		6.79×10^4	A m^{-2}
Kinetic and transport properties	Charge-transfer coefficient, α_a, α_c	0.5, 0.5		0.5, 0.5	
	Solid phase diffusion coefficient, D_s	Ds = f(T)			m^2 s^{-1}
	Solid phase conductivity, σ	100		1	S m^{-1}
	Electrolyte phase Li^+ diffusion coefficient, D_e	De = f(T)			m^2 s^{-1}
	Bruggeman's porosity exponent, p	1.5	1.5	1.5	
	Electrolyte phase ionic conductivity, κ	$\kappa = 1106c_e \exp(-8900c_e^{1.4})$			S m^{-1}
	Li^+ transference number, t_0^+	0.363	0.363	0.363	
	Equilibrium potential of LFP	$U_{equ+}(y) = 3.4323 + 0.8428\exp(-80.2493y^{1.3198}) + 3.2474 \times 10^{-6}\exp(20.2645y^{3.8003}) - 3.2482 \times 10^{-6}\exp(20.2646y^{3.7995})$			

Table 9
Model parameters for EoL.

Parameter	Value	Source
Exchange current density of side reaction, $i_{0,side}$ (A m^{-2})	2.28×10^{-7} at 25 °C 2.62×10^{-7} at 40 °C 2.73×10^{-7} at 55 °C	Optimized by comparing simulation to the self-discharge data
Standard equilibrium potential of side reaction, $U^{\Theta}_{equ,side}$ (V)	0.2	Optimized by comparing simulation to the experimental data
Molar volume of SEI, $\tilde{V}_{SEI}$ (mol m^{-3})	2×10^6	Obtained by assuming the initial thickness of SEI is 2 nm
Ionic conductivity of SEI, κ_{SEI} (S m^{-1})	4×10^{-7}	Optimized by comparing simulation to the terminal voltage under cycling
isolation rate of active anode materials due to SEI, k_s	15	Optimized by comparing simulation to measured capacity fade
molar volume of DL, $\tilde{V}_{DL}$ (mol m^{-3})	7.56×10^9	Used from literature [33]
ionic conductivity of DL, κ_{DL} (S m^{-1})	0.1	Optimized by comparing simulation to the terminal voltage under cycling
molar volume of electrolyte, $\tilde{V}_e$ (mol m^{-3})	3.25×10^8	Optimized by comparing simulation to the terminal voltage under cycling

$$\Delta\varepsilon_s = -k_s a_s \delta_{SEI} \tag{25}$$

where ε_s is the volume fraction of the active electrode material, and k_s is a dimensionless coefficient.

The increasing rate of the thickness and impedance of the DL are described in Eq. (26) and Eq. (27).

$$\frac{\partial\delta_{DL}}{\partial t} = -\frac{R_s\tilde{V}_{DL}}{2F} j^{Li}_{side,x=\delta_-} \tag{26}$$

$$\Delta R_{DL} = \delta_{DL}/\kappa_{DL} \tag{27}$$

Where δ_{DL}, $\tilde{V}_{DL}$ and κ_{DL} are the thickness, molar volume and ion conductivity of the DL, respectively.

4. Results and discussion

Some of geometric and morphologic parameters of the cells, such as thickness, particle radius, active material volume fraction etc., are provided by the manufacturer, while the others, such as stoichiometric number and diffusion coefficients of solid and electrolyte phase etc., are used from literatures and then optimized based on the validated results. The list of the parameters for BoL and EoL can be found in Tables 8 and 9, respectively. The parameters except for some temperature-dependent ones, such as diffusion coefficients and exchange current density of side reaction, are the same in the development of the integrated electrochemical model. The temperature-dependent parameters are optimized by the means of the Arrhenius equation.

4.1. Validation for beginning-of-life (BoL)

In order to verify the accuracy of the ROM with EKF, the experimental data and their corresponding simulation results with different discharge/charge currents applied are compared at different operating temperatures. The comparison of the discharge profile between the simplified ROM and the ROM with EKF is depicted in Fig. 4(a). The constant discharging current of 1C-rate with resting is applied to a fresh LFP/graphite cell at the operating temperature of 25 °C. The markers, the pink solid line and the blue solid line represent the results of experiments, ROM and ROM with EKF, respectively. For the constant discharging, the terminal voltage of both the ROM and the ROM with EKF shows a good match with the experimental data. However, the ROM could not reach the EoD cutoff voltage. Furthermore, the prediction of voltage recovery during resting is underestimated by the ROM, but in an excellent match with the ROM with EKF. Therefore, the incorporation of the EKF into the developed ROM achieves a high accuracy of the estimation of the terminal voltage and SoC.

The comparisons of terminal voltage and SoC between

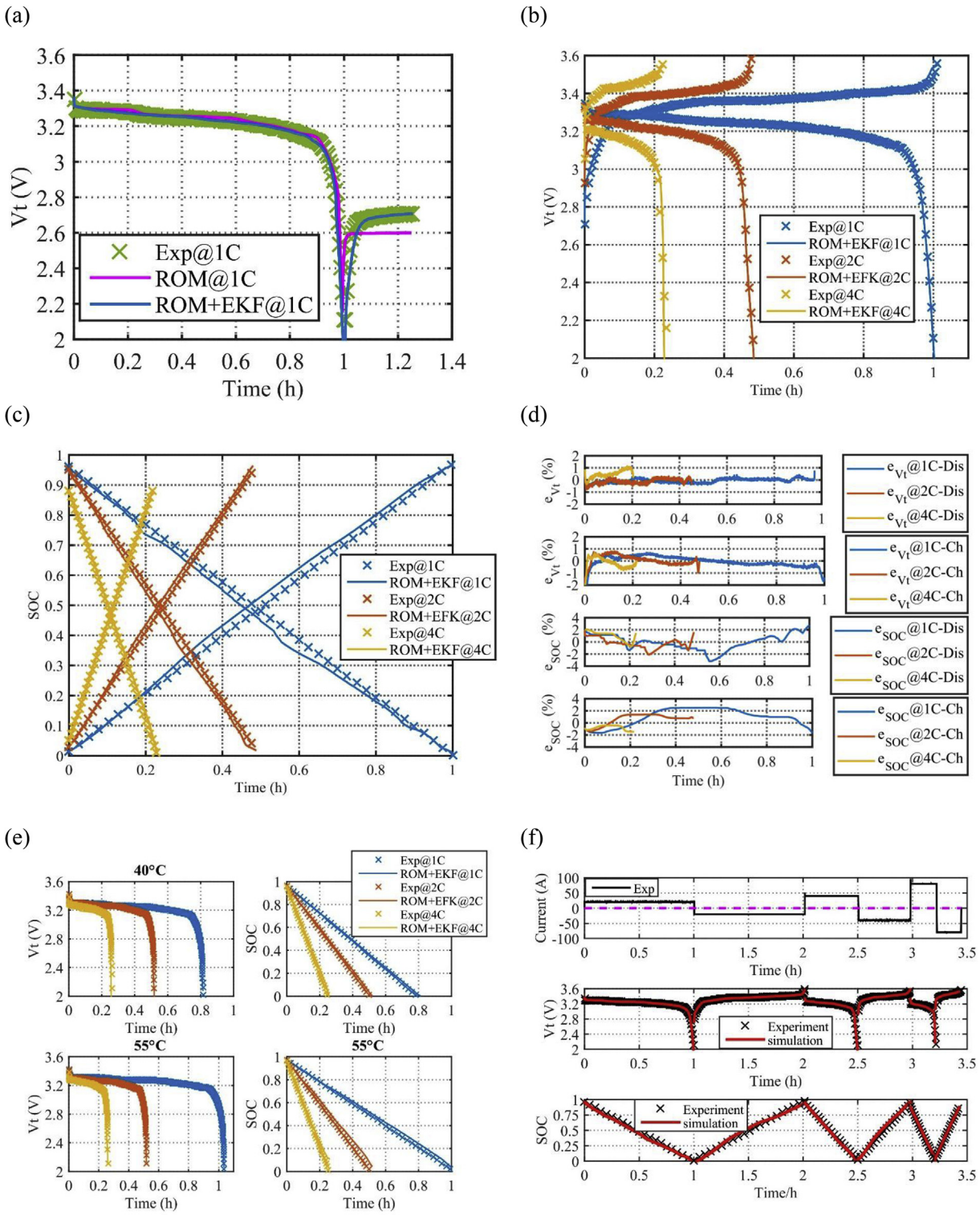

Fig. 4. Validation for BoL at different conditions. (a) Comparison of discharge behaviors between experimental data and simulation results of ROM with/without EKF at 25 °C; (b) Comparison of terminal voltage at 25 °C; (c) Comparison of SoC at 25 °C; (d) Voltage and SoC estimation error at 25 °C; (e) Comparison of terminal voltage and SoC at 40/55 °C; (f) Comparison of terminal voltage and SoC for multiple cycles at 25 °C.

experimental data and simulation results of the ROM with EKF at different discharge and charge currents (1/2/4C-rate) applied at 25 °C are plotted in Fig. 4(b) and (c), respectively. Since constant currents are applied to the cells, the slope of the SoC should be a constant. The markers and the solid lines represent the experiments and simulations, respectively. The responses of terminal voltages and SoCs have a good match with experiments of different discharge and charge profiles at 25 °C. The error between the experimental measurements and the estimated results obtained from the ROM with EKF are summarized and depicted in

Fig. 4(d). The estimated errors of terminal voltage and SoC under different discharging and charging conditions are within 2% and 4%, respectively.

Some parameters of the ROM are highly sensitive to the temperatures, such as the diffusion coefficients of solid and electrolyte phase. According to the analysis of parameter sensitivity, the diffusion coefficient of solid phase has affected the capacity, while that of the electrolyte phase has affected the over-potential. Thus, dependency of the diffusion coefficients of solid and electrolyte phase on temperature are reflected using the Arrhenius equation. Different discharging currents (1/2/4C) are applied to the cells at 40 °C and 55 °C. The comparison results of terminal voltage and SoC are plotted in Fig. 4(e). The upper two subplots in Fig. 4(e) are the comparisons of terminal voltage and SoC at 40 °C from left to right, while the lower two subplots are those at 55 °C, respectively. Both terminal voltage and SoC estimations are in a good match.

Besides the validation of the static response of the integrated ROM with EKF, such as constant discharging and constant charging, the transient response of the model is validated against multiple cycles. The upper subplot in Fig. 4(f) depicts the load current profiles to the cells. The positive and negative sign of the current is defined as the discharging and charging current, respectively. The middle subplot is the response of terminal voltage at multiple cycles at 25 °C. The bottom subplot is then the SoC comparison between experiments and simulations at 25 °C. The makers, 'X', and solid line represent the experimental measurements and simulation results, respectively. Furthermore, the simulation results show a great match with experimental measurements.

4.2. Analysis of degradation effects

Since the LFP/graphite cells discussed in the paper is difficult to get aged, the degradation effects of side reaction rate and other corresponding parameters, such as volume fraction of electrode and electrolyte, resistance of the SEI and DL, ion loss and AM loss, can be analyzed by the validation results at 55 °C. The change of degradation related parameters over time are calculated by the equations in section 3.3.2. The distribution of side reaction rate along the direction of anode thickness as a function of cycle number is depicted in Fig. 5(a). The x-axis and y-axis denote the dimensionless anode thickness and side reaction rate, respectively. The dimensionless anode thickness, $\delta_- = 0$ and $\delta_- = 1$, illustrates the location of the interface between copper current collector and the composite anode and that between the composite anode and separator, respectively. The analysis has shown that side reaction rate at the interface between the composite anode and the separator is higher due to the higher ion concentration. The lithium ions are accumulated at the interface of the separator in a charging period, which promotes the side reaction and results in the formation of the DL. In addition, as the number of cycles increases, the

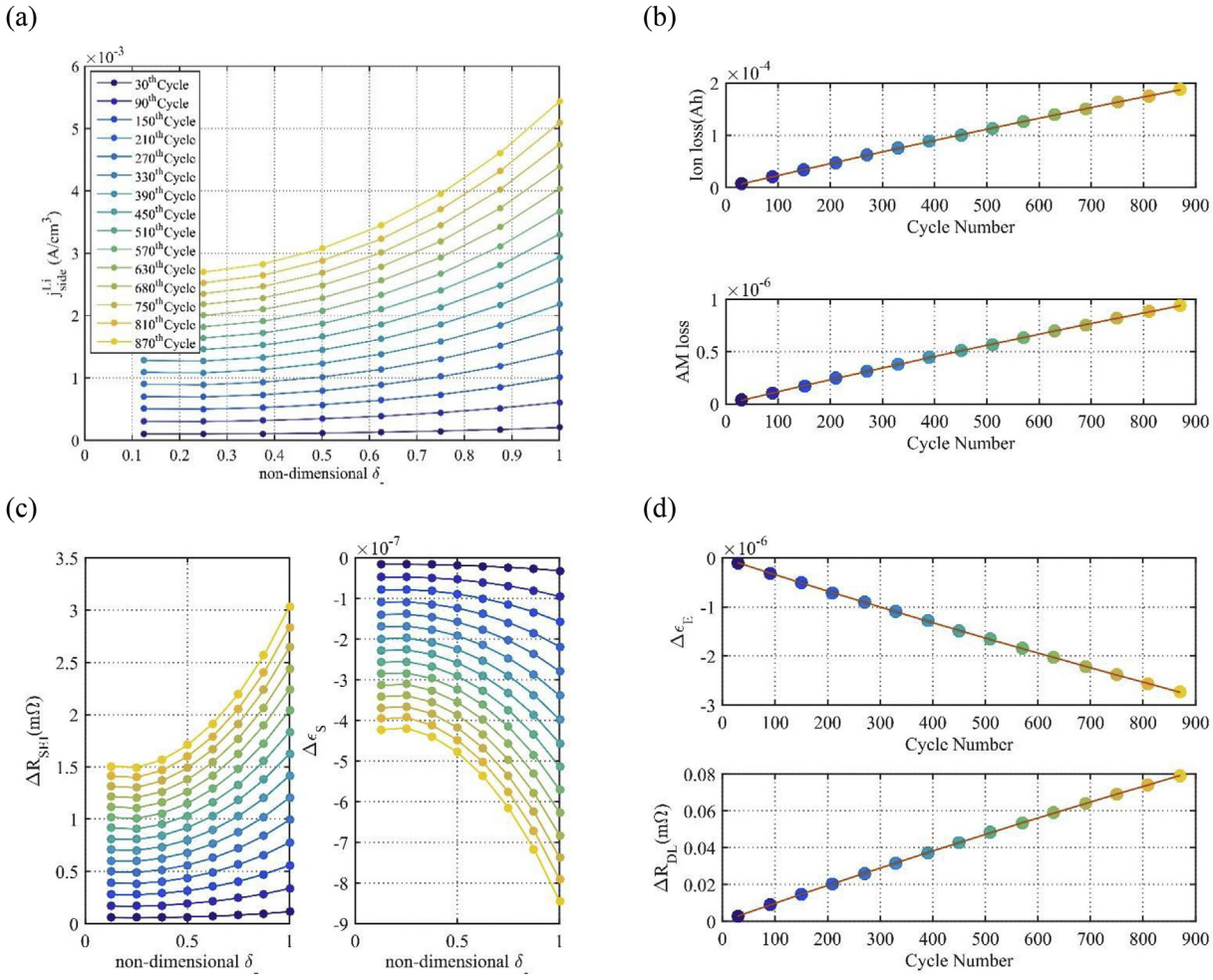

Fig. 5. Analysis of degradation parameters during side reaction. (a) Side reaction rate; (b) Ion loss and AM loss; (c) Change of SEI resistance and volume fraction of anode; (d) Change of electrolyte volume fraction and resistance of DL.

Table 10
Degradation effects and parameters of side reaction.

Causes	Effects	Degradation parameters	Consequences
Side reaction rate $\left\|j_{side}^{Li}\right\|\uparrow$	Loss of recyclable lithium ions	$q_{side}^{Li}(t)\uparrow$	Capacity fade
	Loss of active anode material	Electrode volume fraction $\varepsilon_s\downarrow$	Capacity fade
	Growth of SEI	SEI resistance $R_{SEI}\uparrow$	Impedance rise
	Growth of DL	DL resistance $R_{DL}\uparrow$	Impedance rise
	Electrolyte decomposition	Electrolyte volume fraction $\varepsilon_e\downarrow$	Impedance rise

side reaction rate increases as well, which induces the growth of SEI.

The side reaction consumes recyclable lithium ions (q_{side}^{Li}), which causes loss of ions. The growth of SEI layer can clog pores and isolate particles so that the accessible area gets reduced, which is accelerated by increasing number of cycles as shown in Fig. 5(b). The variation of SEI resistance and electrode volume fraction over time along the anode thickness direction is plotted in Fig. 5(c), while that of electrolyte volume fraction and resistance of the DL as a function of cycle number is plotted in Fig. 5(d). Accordingly, the resistance of SEI (R_{SEI}) increases, while the electrode volume fraction (ε_s) decreases over time.

According to the side reaction describing by Eqs. (1) and (2), the electrolyte, as one of the reactants, is consumed continuously, which leads to the decrease of electrolyte volume fraction (ε_e). The thickness of the DL increases over time, so that the resistance of DL (R_{DL}) increases with the increasing cycle number. The analysis of the degradation effects of side reaction based on the variation of the electrochemical parameters can be summarized in Table 10.

4.3. Validation of end-of-life (EoL)

Compared with the effects of temperature, those of SoC cycling limit, SoC level and charging C-rate have less influence on the degradation of LFP/graphite cells [31]. Thus, temperature, as the key factor of accelerating degradation, will be investigated in more details. The comparison of discharge terminal voltage with 1C-rate discharge current applied between simulation results obtained by the physics-based degradation model and experimental data at different operating temperatures are plotted from Fig. 6(a) to Fig. 6(c). As the cells are aged with the increase of number of cycles, the time to reach EoD voltage has been reduced. The prediction of terminal voltage during discharge is estimated up to 1080, 900 and 870 cycles at 25 °C, 40 °C and 55 °C, respectively.

Capacity fade is one of the most significant criteria to evaluate performance of degraded LiBs, which is mainly caused by ion loss and AM loss. The comparison of simulated capacity and the Ah-based measured capacity as the function of cycle number is shown in the upper subplot of Fig. 7. Furthermore, the corresponding error between measurements and simulation results is plotted in the lower subplot. In order to display the capacity variations comparably, the dimensionless capacity retention is defined as the capacity ratio of the aged cell over the fresh cell in Eq. (28). The relative capacity error is calculated by Eq. (29).

$$Q_{\text{max}-\text{dimensionless}} = \frac{Q_{aged,cell}}{Q_{fresh,cell}} \times 100\% \tag{28}$$

$$Q_{error-\text{dimensionless}} = \frac{Q_{\text{exp}} - Q_{sim}}{Q_{\text{exp}}} \times 100\% \tag{29}$$

The color of purple and red, orange and yellow, and cyan and blue in the upper subplot of Fig. 7 denotes the capacity retention calculated based on experimental data and simulation results at 25 °C, 40 °C and 55 °C, respectively. The error shown in the lower

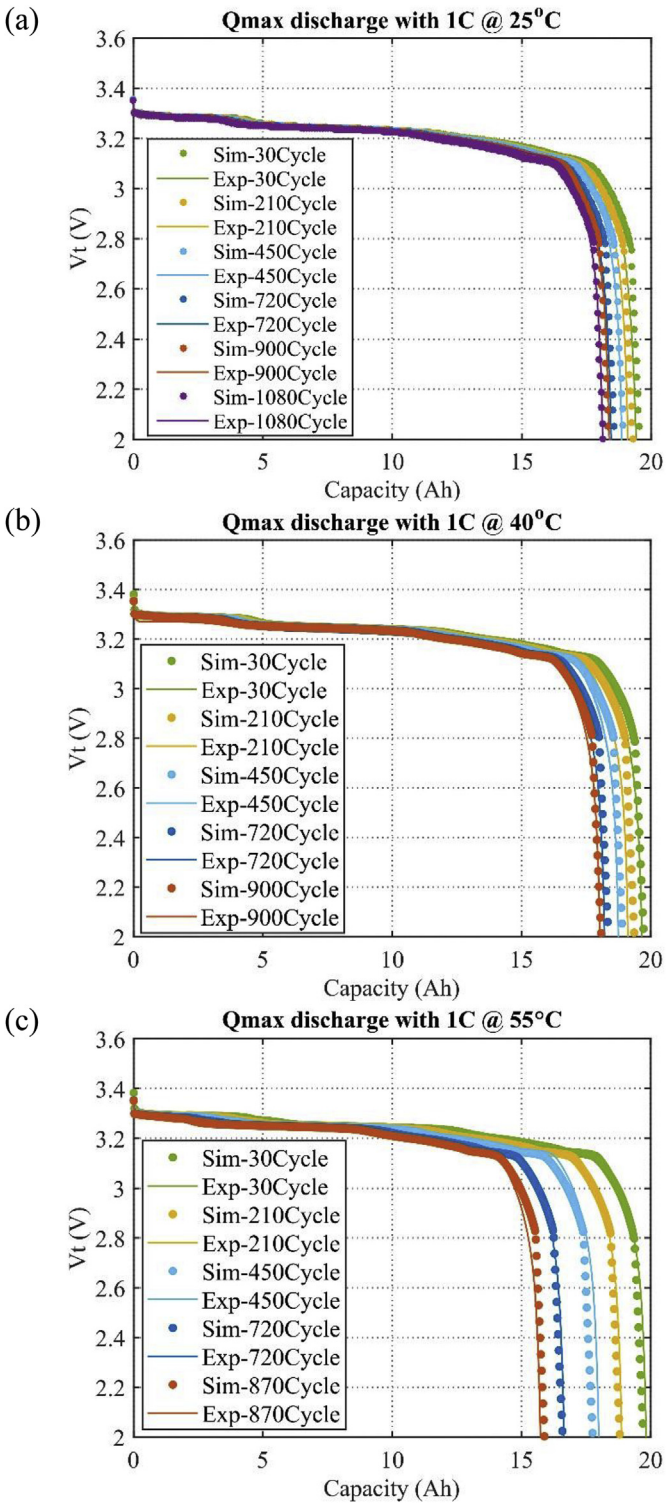

Fig. 6. Validation of discharge behaviors by 1C-rate current at 25/40/55 °C. (a) 25 °C; (b) 40 °C; (c) 55 °C.

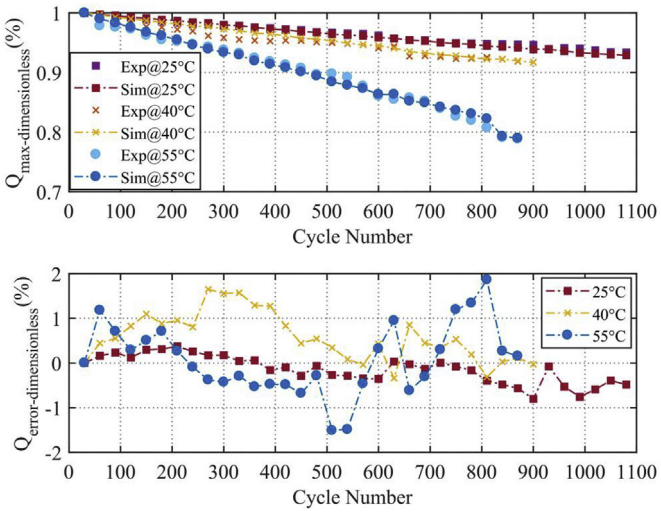

Fig. 7. Comparison between Ah-based measured capacity and simulated capacity at 25/40/55 °C.

subplot of Fig. 7 is within 1%, 2%, and 2% at 25 °C, 40 °C and 55 °C, respectively.

The other major consequence of degradation is the rise of impedances that leads to power fade. The ion-consuming SEI and DL growth and the dryness of electrolyte due to side reaction result in the power fade. In order to obtain the SEI resistance, the impedance spectra of cells cycled at 25 °C and 55 °C are plotted in Fig. 8(a) and (b), respectively. As the increase of cycle number, the radius of the first semi-circle on behalf of SEI resistance is increased, especially at the elevated temperature. The SEI resistance extracted from the ECM based on the EIS experimental data is compared with the simulated results obtained from the integrated degradation model at different operating temperatures, which is shown in Fig. 8(c). The markers of cross and circle represent experimental data and simulation results, respectively. The growth of SEI resistance matches well with each other. The comparison manifests that elevated operating temperature accelerates the degradation of LFP/graphite cells. Power fade is predicted at different operating temperatures as shown in Fig. 9. The upper subplot displays the comparison of power between measurements and simulations at different operating temperatures. The lower subplot presents the corresponding error of power at 25 °C and 55 °C, respectively. With consideration of the change of ionic conductivity of SEI and DL, the

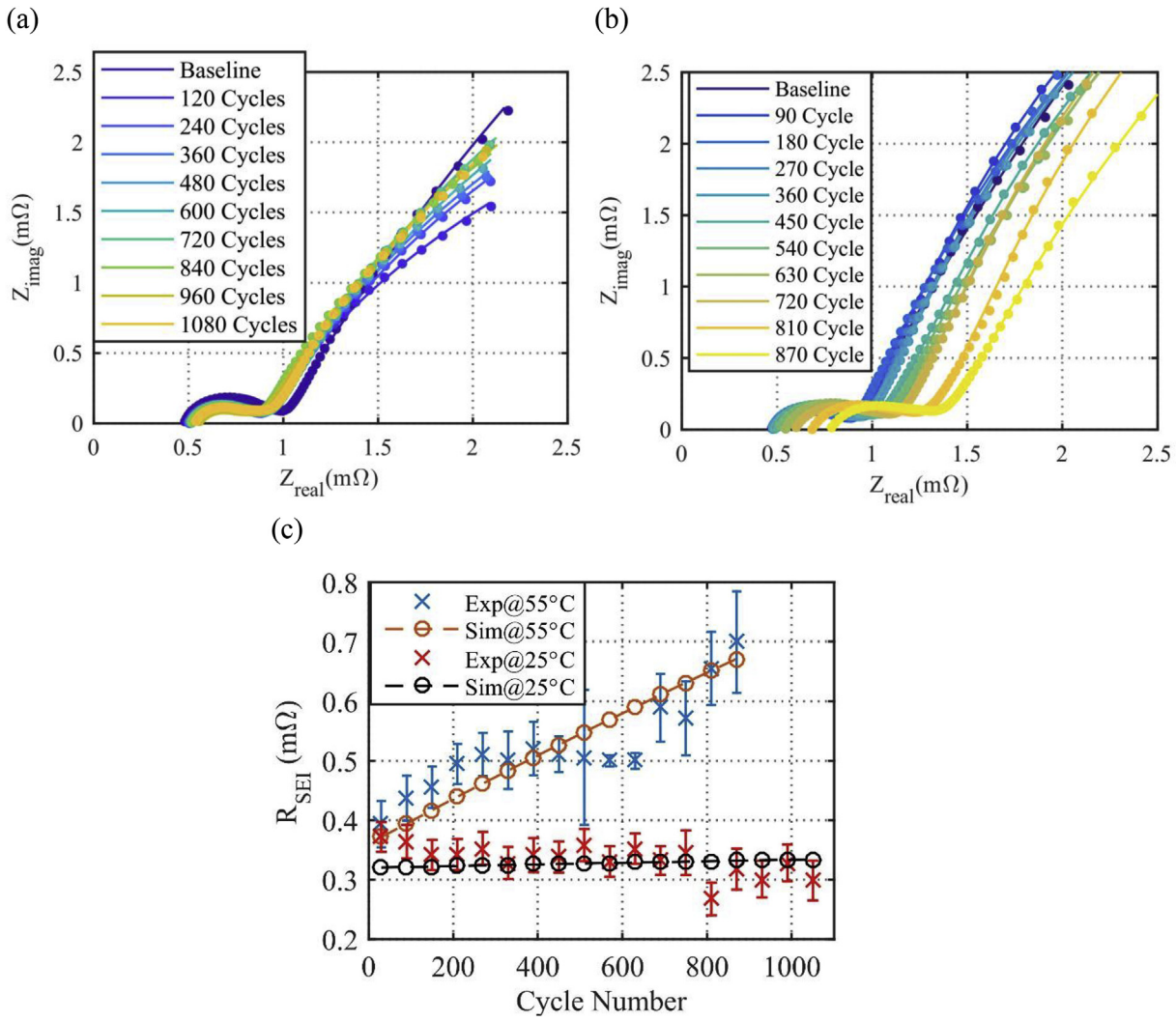

Fig. 8. Comparison of EIS spectra and SEI resistance at different temperatures with increasing cycle number. (a) EIS spectra of the cell cycled at 25 °C with SoC cycling limits from 25% to 95%; (b) EIS spectra of the cell cycled at 55 °C with SoC cycling limits from 25% to 95%; (c) SEI resistance.

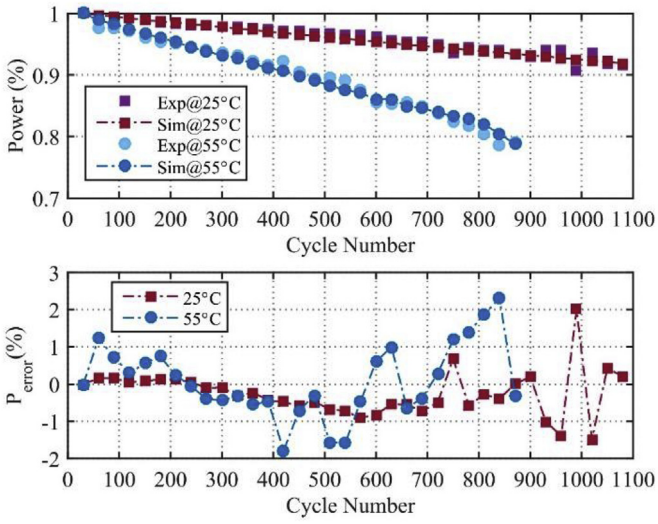

Fig. 9. Comparison power fade at different temperatures with increasing cycle number.

power decreases as the increase of cycle number. The overall error of power estimation is within 3%.

5. Conclusion

An integrated ROM that includes EKF for enhancing estimation accuracy of terminal voltage and SoC for BoL as well as a life model that facilitates capacity and power fade for EoL is developed. The model is validated against both fresh and cycled pouch-type large-format LFP/graphite cells, whose nominal capacity is 20Ah. The unique characteristics of ion behaviors in the cathode particles including two-phase transition and path dependence are described using a shrinking core model. The EKF is incorporated into the developed ROM to achieve a higher accuracy of terminal voltage and SoC estimation. With different discharging and charging profiles applied to the cells, including both single cycles and multiple cycles, the electrochemical behaviors of the cells are explored at different working temperatures. The temperature dependent parameters, such as diffusion coefficients of solid and electrolyte phase, are formulated using the Arrhenius equation. The average error of terminal voltage and SoC estimation is within 2% and 4%, respectively.

According to the experimental studies on degradation mechanism, the side reaction has been identified as the predominant cause for both calendar and cycle life, which is accelerated by the elevated operating temperatures, high SoC levels and large SoC cycling limits. These phenomena are formulated by modifying BV equation that is incorporated into the ROM with EKF. The capacity fade is caused by loss of recyclable lithium ions and loss of AM, while the power fade is the growth of SEI and DL and electrolyte decomposition. The ROM with EKF and life model is validated by the accelerated cycling tests conducted at various operating conditions, including working temperatures, SoC cycling limits and SoC levels, which match well with experimental data with respect to terminal voltage, capacity fade and power fade. The estimation error of capacity and power as the function of cycle number at different temperatures have been remained within 2% and 3%, respectively.

Future work will include the development of a subzero temperature electrochemical model that considers the effects of lithium plating/stripping at different working conditions.

Acknowledgement

The authors gratefully acknowledge the financial and technical support from Korea Electric Power Corporation and specially would also like to express our thanks to Top Battery for providing the LFP/graphite cells.

References

[1] A.K. Padhi, K.S. Nanjundaswamy, J.B. Goodenough, Phospho-olivines as positive-electrode materials for rechargeable lithium batteries, J. Electrochem. Soc. 144 (1997) 1188–1194, https://doi.org/10.1684/agr.2014.0700.
[2] M. Safari, C. Delacourt, Modeling of a commercial graphite/$LiFePO_4$ cell, J. Electrochem. Soc. 158 (2011) A562–A571, https://doi.org/10.1149/1.3567007.
[3] V. Srinivasan, J. Newman, Discharge Model for the lithium iron-phosphate electrode, J. Electrochem. Soc. 151 (2004) A1517–A1529, https://doi.org/10.1149/1.1785012.
[4] C. Wang, U.S. Kasavajjula, P.E. Arce, A discharge model for phase transformation electrodes: formulation, experimental validation, and analysis, J. Phys. Chem. C 111 (2007) 16656–16663, https://doi.org/10.1021/jp074490u.
[5] U.S. Kasavajjula, C. Wang, P.E. Arce, Discharge Model for $LiFePO_4$ accounting for the solid solution range, J. Electrochem. Soc. 155 (2008) A866–A874, https://doi.org/10.1149/1.2980420.
[6] A. Khandelwal, K.S. Hariharan, V. Senthil Kumar, P. Gambhire, S.M. Kolake, D. Oh, S. Doo, Generalized moving boundary model for charge-discharge of $LiFePO_4$/C cells, J. Power Sources 248 (2014) 101–114, https://doi.org/10.1016/j.jpowsour.2013.09.066.
[7] M. Safari, C. Delacourt, Mathematical modeling of lithium iron phosphate electrode: galvanostatic charge/discharge and path dependence, J. Electrochem. Soc. 158 (2011) A63–A73, https://doi.org/10.1149/1.3515902.
[8] T.-S. Dao, C.P. Vyasarayani, J. McPhee, Simplification and order reduction of lithium-ion battery model based on porous-electrode theory, J. Power Sources 198 (2012) 329–337, https://doi.org/10.1016/j.jpowsour.2011.09.034.
[9] N. Baba, H. Yoshida, M. Nagaoka, C. Okuda, S. Kawauchi, Numerical simulation of thermal behavior of lithium-ion secondary batteries using the enhanced single particle model, J. Power Sources. 252 (2014) 214–228, https://doi.org/10.1016/j.jpowsour.2013.11.111.
[10] K.A. Smith, C.D. Rahn, C.-Y. Wang, Model order reduction of 1D diffusion systems via residue grouping, J. Dyn. Syst. Meas. Contr. 130 (2008), https://doi.org/10.1115/1.2807068, 11012-1-11012–8.
[11] V.R. Subramanian, V. Boovaragavan, V. Ramadesigan, M. Arabandi, Mathematical model reformulation for lithium-ion battery simulations: galvanostatic boundary conditions, J. Electrochem. Soc. 156 (2009) A260–A271, https://doi.org/10.1149/1.3065083.
[12] L. Cai, R.E. White, Reduction of model order based on proper orthogonal decomposition for lithium-ion battery simulations, J. Electrochem. Soc. 156 (2009) A154–A161, https://doi.org/10.1149/1.3049347.
[13] V.S. Kumar, Reduced order model for a lithium ion cell with uniform reaction rate approximation, J. Power Sources 222 (2013) 426–441, https://doi.org/10.1016/jjpowsour.2012.09.013.
[14] M. Kassem, J. Bernard, R. Revel, S. Pélissier, F. Duclaud, C. Delacourt, Calendar aging of a graphite/$LiFePO_4$ cell, J. Power Sources 208 (2012) 296–305, https://doi.org/10.1016/j.jpowsour.2012.02.068.
[15] R.P. Ramasamy, R.E. White, B.N. Popov, Calendar life performance of pouch lithium-ion cells, J. Power Sources 141 (2005) 298–306, https://doi.org/10.1016/j.jpowsour.2004.09.024.
[16] M. Dubarry, V. Svoboda, R. Hwu, B. Yann Liaw, Incremental Capacity analysis and close-to-equilibrium OCV measurements to quantify capacity fade in commercial rechargeable lithium batteries, Electrochem. Solid State Lett. 9 (2006) A454–A457, https://doi.org/10.1149/1.2221767.
[17] J. Wang, P. Liu, J. Hicks-Garner, E. Sherman, S. Soukiazian, M. Verbrugge, H. Tataria, J. Musser, P. Finamore, Cycle-life model for graphite-$LiFePO_4$ cells, J. Power Sources 196 (2011) 3942–3948, https://doi.org/10.1016/j.jpowsour.2010.11.134.
[18] H.-F. Jin, Z. Liu, Y.M. Teng, J. kui Gao, Y. Zhao, A comparison study of capacity degradation mechanism of $LiFePO_4$-based lithium ion cells, J. Power Sources 189 (2009) 445–448, https://doi.org/10.1016/j.jpowsour.2008.12.124.
[19] J. Schmalstieg, S. Käbitz, M. Ecker, D.U. Sauer, A holistic aging model for $Li(NiMnCo)O_2$ based 18650 lithium-ion batteries, J. Power Sources 257 (2014) 325–334, https://doi.org/10.1016/j.jpowsour.2014.02.012.
[20] P. Ramadass, B. Haran, P.M. Gomadam, R.E. White, B.N. Popov, Development of first principles capacity fade model for Li-ion cells, J. Electrochem. Soc. 151 (2004) A196–A203, https://doi.org/10.1149/1.1634273.
[21] S. Santhanagopalan, Q. Zhang, K. Kumaresan, R.E. White, Parameter estimation and life modeling of lithium-ion cells, J. Electrochem. Soc. 155 (2008) A345–A353, https://doi.org/10.1149/1.2839630.
[22] G. Sikha, B.N. Popov, R.E. White, Effect of porosity on the capacity fade of a lithium-ion battery, J. Electrochem. Soc. 151 (2004) A1104–A1114, https://doi.org/10.1149/1.1759972.
[23] H.J. Ploehn, P. Ramadass, R.E. White, Solvent diffusion model for aging of

lithium-ion battery cells, J. Electrochem. Soc. 151 (2004) A456–A462, https://doi.org/10.1149/1.1644601.
[24] Q. Zhang, R.E. White, Capacity fade analysis of a lithium ion cell, J. Power Sources 179 (2008) 793–798, https://doi.org/10.1016/j.jpowsour.2008.01.028.
[25] Y. Zhang, C.-Y. Wang, X. Tang, Cycling degradation of an automotive $LiFePO_4$ lithium-ion battery, J. Power Sources 196 (2011) 1513–1520, https://doi.org/10.1016/j.jpowsour.2010.08.070.
[26] J. Groot, M. Swierczynski, A.I. Stan, S.K. Kær, On the complex ageing characteristics of high-power $LiFePO_4$/graphite battery cells cycled with high charge and discharge currents, J. Power Sources 286 (2015) 475–487, https://doi.org/10.1016/j.jpowsour.2015.04.001.
[27] P. Verma, P. Maire, P. Novák, A review of the features and analyses of the solid electrolyte interphase in Li-ion batteries, Electrochim. Acta 55 (2010) 6332–6341, https://doi.org/10.1016/j.electacta.2010.05.072.
[28] M. Safari, C. Delacourt, Aging of a commercial graphite/$LiFePO_4$ cell, J. Electrochem. Soc. 158 (2011) A1123–A1135, https://doi.org/10.1149/1.3614529.
[29] J. Vetter, P. Novák, M.R. Wagner, C. Veit, K.C. Möller, J.O. Besenhard, M. Winter, M. Wohlfahrt-Mehrens, C. Vogler, A. Hammouche, Ageing mechanisms in lithium-ion batteries, J. Power Sources 147 (2005) 269–281, https://doi.org/10.1016/j.jpowsour.2005.01.006.
[30] A. Barré, B. Deguilhem, S. Grolleau, M. Gérard, F. Suard, D. Riu, A review on lithium-ion battery ageing mechanisms and estimations for automotive applications, J. Power Sources 241 (2013) 680–689, https://doi.org/10.1016/j.jpowsour.2013.05.040 Review.
[31] R. Fu, S.Y. Choe, V. Agubra, J. Fergus, Development of a physics-based degradation model for lithium ion polymer batteries considering side reactions, J. Power Sources. 278 (2015) 506–521, https://doi.org/10.1016/j.jpowsour.2014.12.059.
[32] K. Striebel, A. Guerfi, J. Shim, M. Armand, M. Gauthier, K. Zaghib, $LiFePO_4$/gel/natural graphite cells for the BATT program, J. Power Sources (2003) 951–954, https://doi.org/10.1016/S0378-7753(03)00295-7.
[33] K. Striebel, J. Shim, V. Srinivasan, J. Newman, Comparison of $LiFePO_4$ from different sources, J. Electrochem. Soc. 152 (2005) A664–A670, https://doi.org/10.1149/1.1862477.
[34] K. Amine, J. Liu, I. Belharouak, High-temperature storage and cycling of C-$LiFePO_4$/graphite Li-ion cells, Electrochem. Commun. 7 (2005) 669–673, https://doi.org/10.1016/j.elecom.2005.04.018.
[35] K. Zaghib, N. Ravet, M. Gauthier, F. Gendron, A. Mauger, J.B. Goodenough, C.M. Julien, Optimized electrochemical performance of $LiFePO_4$ at 60°C with purity controlled by SQUID magnetometry, J. Power Sources 163 (2006) 560–566, https://doi.org/10.1016/j.jpowsour.2006.09.030.
[36] P. Liu, J. Wang, J. Hicks-Garner, E. Sherman, S. Soukiazian, M. Verbrugge, H. Tataria, J. Musser, P. Finamore, Aging mechanisms of $LiFePO_4$ batteries deduced by electrochemical and structural analyses, J. Electrochem. Soc. 157 (2010) A499–A507, https://doi.org/10.1149/1.3294790.
[37] H. Ekstrom, G. Lindbergh, A model for predicting capacity fade due to SEI formation in a commercial graphite/$LiFePO_4$ cell, J. Electrochem. Soc. 162 (2015) A1003–A1007, https://doi.org/10.1149/2.0641506jes.
[38] G. Ning, B. Haran, B.N. Popov, Capacity fade study of lithium-ion batteries cycled at high discharge rates 117 (2003) 160–169, https://doi.org/10.1016/S0378-7753(03)00029-6.
[39] M. Safari, M. Morcrette, A. Teyssot, C. Delacourt, Multimodal physics-based aging model for life prediction of Li-ion batteries, J. Electrochem. Soc. 156 (2009) A145–A153, https://doi.org/10.1149/1.3043429.
[40] N. Omar, M.A. Monem, Y. Firouz, J. Salminen, J. Smekens, O. Hegazy, H. Gaulous, G. Mulder, P. Van den Bossche, T. Coosemans, J. Van Mierlo, Lithium iron phosphate based battery - assessment of the aging parameters and development of cycle life model, Appl. Energy 113 (2014) 1575–1585, https://doi.org/10.1016/j.apenergy.2013.09.003.
[41] P. Gambhire, K.S. Hariharan, A. Khandelwal, S.M. Kolake, T. Yeo, S. Doo, A physics based reduced order aging model for lithium-ion cells with phase change, J. Power Sources 270 (2014) 281–291, https://doi.org/10.1016/j.jpowsour.2014.07.127.
[42] C. Kupper, W.G. Bessler, Multi-scale thermo-electrochemical modeling of performance and aging of a $LiFePO_4$/graphite lithium-ion cell, J. Electrochem. Soc. 164 (2017) A304–A320, https://doi.org/10.1149/2.0761702jes.
[43] R. Darling, J. Newmann, Modeling side reactions in composite $LiyMn_2O_4$ electrodes, J. Electrochem. Soc. 145 (1998) 990–998, https://doi.org/10.1149/1.1838376.
[44] C. Delacourt, M. Safari, Life simulation of a graphite/$LiFePO_4$ cell under cycling and storage, J. Electrochem. Soc. 159 (2012) A1283–A1291, https://doi.org/10.1149/2.049208jes.
[45] M. Safari, C. Delacourt, Simulation-Based Analysis of aging phenomena in a commercial graphite/$LiFePO_4$ cell, J. Electrochem. Soc. 158 (2011) A1436–A1447, https://doi.org/10.1149/2.103112jes.
[46] X. Li, M. Xiao, S.Y. Choe, W.T. Joe, Modeling and analysis of $LiFePO_4$/carbon battery considering two-phase transition during galvanostatic charging/discharging, Electrochim. Acta 155 (2015) 447–457, https://doi.org/10.1016/j.electacta.2014.12.034.